






Exotic swarming dynamics of high-dimensional swarmalatorsAkash Yadav ¹, Krishnanand J ¹, V. K. Chandrasekar ^{2,†}, Wei Zou,³ Jürgen Kurths ^{4,5,6} and D. V. Senthilkumar ^{1,*}¹*School of Physics, Indian Institute of Science Education and Research Thiruvananthapuram, Kerala 695551, India*²*Center for Nonlinear Science and Engineering, SASTRA Deemed University, Thanjavur, Tamil Nadu 613401, India*³*School of Mathematical Sciences, South China Normal University, Guangzhou 510631, China*⁴*Potsdam Institute for Climate Impact Research, Telegraphenberg, D-14415 Potsdam, Germany*⁵*Institute of Physics, Humboldt University Berlin, D-12489 Berlin, Germany*⁶*Research Institute of Intelligent Complex Systems, Fudan University, Shanghai 200433, China*

(Received 8 January 2024; accepted 28 March 2024; published 24 April 2024)

Swarmalators are oscillators that can swarm as well as sync via a dynamic balance between their spatial proximity and phase similarity. Swarmalator models employed so far in the literature comprise only one-dimensional phase variables to represent the intrinsic dynamics of the natural collectives. Nevertheless, the latter can indeed be represented more realistically by high-dimensional phase variables. For instance, the alignment of velocity vectors in a school of fish or a flock of birds can be more realistically set up in three-dimensional space, while the alignment of opinion formation in population dynamics could be multidimensional, in general. We present a generalized D -dimensional swarmalator model, which more accurately captures self-organizing behaviors of a plethora of real-world collectives by self-adaptation of high-dimensional spatial and phase variables. For a more sensible visualization and interpretation of the results, we restrict our simulations to three-dimensional spatial and phase variables. Our model provides a framework for modeling complicated processes such as flocking, schooling of fish, cell sorting during embryonic development, residential segregation, and opinion dynamics in social groups. We demonstrate its versatility by capturing the maneuvers of a school of fish, qualitatively and quantitatively, by a suitable extension of the original model to incorporate appropriate features besides a gallery of its intrinsic self-organizations for various interactions. We expect the proposed high-dimensional swarmalator model to be potentially useful in describing swarming systems and programmable and reconfigurable collectives in a wide range of disciplines, including the physics of active matter, developmental biology, sociology, and engineering.

DOI: [10.1103/PhysRevE.109.044212](https://doi.org/10.1103/PhysRevE.109.044212)**I. INTRODUCTION**

The aim of complex systems science is to understand the underlying dynamical processes that are responsible for a plethora of self-organizing collective behaviors stemming from microscopic collectives in various branches of science and technology, including systems biology [1,2], climate science [3,4], complex networks [5,6], ecology [7], and social studies [8,9] in an effort towards increasing their resilience and effective utilization. In the field of complex systems science, there has been a recent, growing interest in studies on swarming dynamics that have captured the essential features of several natural collectives and their intrinsic dynamics with potential applications [10–17]. Swarmalators represent a class of systems that can self-aggregate spatially (swarm) and simultaneously adjust their internal rhythms (synchronize) through a delicate balance between their spatial proximity and phase similarity, representing the latter. Pioneering contributions were made by Igosin *et al.* and Tanaka *et al.* in modeling the dynamics of chemotactic oscillators [18–20], and by Levis *et al.* in describing the dynamics of revolving agents [21,22].

The recent surge in swarmalator studies has revealed a plethora of collective dynamical states that mimic the self-organizing dynamics of natural [23,24] and technological [25–27] collectives ranging from spermatozoa [23] to drones and robots [28–30]. A recent study by O’Keeffe *et al.* [10] elucidated that a static phase wave (SPW) is qualitatively similar to the “asters” formed by ferromagnetic colloids [31], whereas an active phase wave (APW) has the characteristic features of “vortex arrays” formed by populations of spermatozoa [23]. Generalization of the swarmalator model [10] by including nonidentical frequencies, chirality, and local coupling unveiled several new spatiotemporal regimes, including interacting phase waves, vortices, and beating clusters [12]. It was also shown that many of these self-organizing patterns resemble qualitatively patterns exhibited by cellular self-organization [32,33], flocking patterns of Quincke rollers [26,34], and the various life stages of slime mold [35]. An attempt was made recently to arrive at an analytical description of the synchronized state and the existence condition for a few of the states using a basic model [16]. Other extensions have been made by including a Gaussian function for short-range repulsive interaction [13], delayed interactions [15], and pinning [17].

One of the prospective applications of reconfigurable swarmalators is their locomotive utility [10]. For instance, the

*skumar@iisertvm.ac.in

†chandru25nld@gmail.com

collective metachronal waves known to facilitate biological transport [36,37] of populations of cilia are similar to APWs and splintered phase waves (SPPWs). In particular, reconfigurable microrobot swarms, a perfect real-world example of swarmalators, can be used for biomedical applications including targeted drug delivery [29,30,38]. Very recently, a swarmalator model was shown to exhibit the essential features of programmable self-organization of heterogeneous micro-robot collectives [39]. It has also been pointed out that no other active matter model is as concise as the minimalistic swarmalator model, which offers such a diverse set of emergent collective behaviors [12].

Given the tremendous potential real-world applications of swarmalators, the model employed in the aforementioned studies invariably comprises evolution equations for two-dimensional spatial variables and the one-dimensional Kuramoto model [40] governing phase dynamics. However, most of these studies generalized their results to three-dimensional spatial variables, where the phase evolves on a unit circle in accordance with spatial proximity, but it lacks an orientational degree of freedom, which is a key component of almost all real-world swarmalators, e.g., spin orientation in ferromagnetic collides [41], velocity vectors of flocks of birds [42,43], schools of fish, swarms of drones, etc. The orientation degree of freedom is an intrinsic feature of all systems described by spherical polar coordinates, in which the orientation vector is specified by both polar angle θ and azimuthal angle ϕ . The internal state of such systems must inevitably be described by the orientation vector represented in terms of θ and ϕ in three dimensions (3D) to represent those systems more accurately (see Fig. 1), which is missing in the existing studies on swarmalators.

To capture the self-organizing spatiotemporal patterns and to understand their underlying mechanisms of the natural collectives more accurately, we introduce here a D -dimensional swarmalator model governed by D -dimensional spatial and D -dimensional orientation vectors, in general, for predictive fidelity of the self-organizing behaviors of real-world collectives, where the alignment of their orientation vectors represents their intrinsic dynamics. For a more sensible visualization and interpretation of the results, we restrict our simulations to 3D spatial and 3D phase variables. We show that in view of the inseparable dynamics of θ and ϕ governing the spatial proximity and vice versa in 3D, our model indeed facilitates a repertoire of exotic self-organizing behaviors (see Table S1) that are specific to our model and generalize those states observed by the aforementioned studies, with similar settings but with only a 1D phase variable representing the intrinsic dynamics to higher dimensions.

II. MODEL DESCRIPTION

The proposed D -dimensional swarmalator model is represented by

$$\dot{\mathbf{x}}_i = \mathbf{v}_i + \frac{1}{N-1} \sum_{j=1}^N \{1 + J(\boldsymbol{\sigma}_i \cdot \boldsymbol{\sigma}_j)\} \frac{\mathbf{x}_j - \mathbf{x}_i}{|\mathbf{x}_j - \mathbf{x}_i|^\alpha} - \frac{\mathbf{x}_j - \mathbf{x}_i}{|\mathbf{x}_j - \mathbf{x}_i|^\beta} + \boldsymbol{\xi}_i^\mathbf{x}(t), \quad (1a)$$

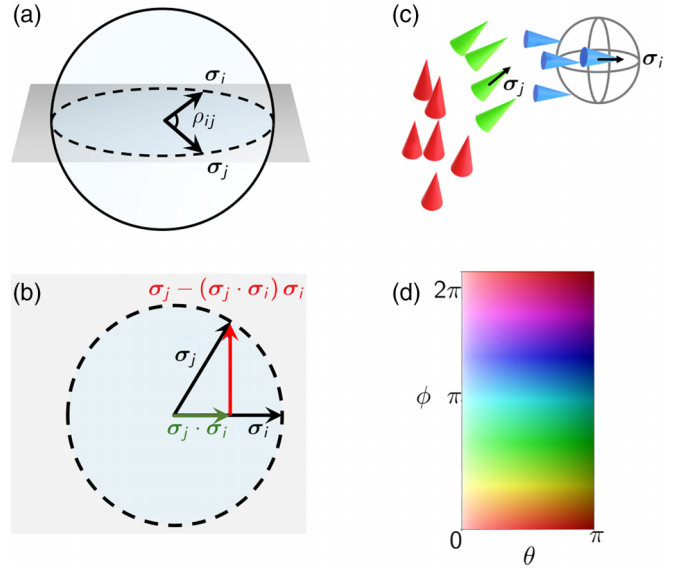


FIG. 1. 3D phase and its visualization. (a) Orientations $\boldsymbol{\sigma}_i$ and $\boldsymbol{\sigma}_j$ of i th and j th swarmalators, respectively, can be represented as vectors pointing on a unit sphere. (b) Deriving the analogs of $\sin(\rho_{ij})$ and $\cos(\rho_{ij})$ in terms of orientation vectors $\boldsymbol{\sigma}_i$ and $\boldsymbol{\sigma}_j$. Here ρ_{ij} is the angle of inclination of orientation vectors, $\cos(\rho_{ij})$ is simply the projection of $\boldsymbol{\sigma}_j$ on $\boldsymbol{\sigma}_i$, and $\sin(\rho_{ij})$ is the y -component of $\boldsymbol{\sigma}_j$. (c) Each swarmalator is represented by a cone with its apex pointing along its orientation vector. (d) The heat map, encoding the degree of orientation of the vectors, which in turn is determined by the polar phase (θ) and the azimuthal phase (ϕ), is used to color the cones in accordance with the distribution of the initial conditions, which facilitates the identification of distinct collective states even when the cones are masked behind a dense set of cones.

$$\dot{\boldsymbol{\sigma}}_i = W_i \boldsymbol{\sigma}_i + \sum_{j=1}^N K_{ij} \left[\frac{\boldsymbol{\sigma}_j - (\boldsymbol{\sigma}_j \cdot \boldsymbol{\sigma}_i) \boldsymbol{\sigma}_i}{|\mathbf{x}_j - \mathbf{x}_i|^\gamma} \right] + \boldsymbol{\xi}_i^\boldsymbol{\sigma}(t), \quad (1b)$$

where $i = 1, 2, 3, \dots, N$ is the number of swarmalators, \mathbf{x}_i is the D -dimensional position vector of the i th swarmalator, $\boldsymbol{\sigma}_i$ is its orientation vector on the D -dimensional unit hypersphere (see Fig. 1) characterizing the intrinsic dynamics of the swarms, and \mathbf{v}_i is its self-propulsion velocity. Note that the evolution equation for $\boldsymbol{\sigma}_i$ in the absence of the distant dependent kernel is the D -dimensional Kuramoto model [43,44] (see Sec. S1 of the Supplemental Material [45] for its derivation). In the context of flocking and swarming models, $\boldsymbol{\sigma}_i$ can be interpreted as the unit vector along the velocity vector of the i th swarmalator [43], while in the context of social interactions, the alignment of opinion dynamics could, in general, be multidimensional [43,44].

The first and second terms in Eq. (1a) correspond to the spatial attraction and repulsion, respectively. Spatial attraction between the swarmalators depends on the degree of orientation and the parameter J . The repulsive interaction is essential to maintain the minimum separation between agents. The nature of the distance-dependent spatial interactions can be tuned with the exponents α , β , and γ . The distant-dependent kernels in Eq. (1a) act like a van der Waals interaction for $\beta > \alpha$ that ensures the long-range attraction and short-range repulsion.

Consequently, altering these parameters will only affect the equilibrium distance between the swarmalators as depicted in Fig. S7. Therefore, the states reported in our study can still be observed across different sets of α , β , and γ values, which may slightly shift their spread in the two-parameter phase diagrams.

W_i is the antisymmetric angular velocity $D \times D$ matrix of the i th swarmalator, which can be represented in 3D as

$$W_i = \begin{pmatrix} 0 & -\omega_{i,3} & \omega_{i,2} \\ \omega_{i,3} & 0 & -\omega_{i,1} \\ -\omega_{i,2} & \omega_{i,1} & 0 \end{pmatrix}, \quad (2)$$

where $\omega_i = (\omega_{i,1}, \omega_{i,2}, \omega_{i,3})$ represents the angular velocity of the i th swarmalator. The coupling strength K_{ij} is given as

$$K_{ij} = \begin{cases} \varepsilon_a/N_i & \text{for } |\mathbf{x}_j - \mathbf{x}_i| \leq R, \\ -\varepsilon_r/N_r & \text{for } |\mathbf{x}_j - \mathbf{x}_i| > R, \end{cases}$$

where ε_a is the attractive phase coupling strength, ε_r is the repulsive phase coupling strength, R is the vision radius, N_i is the number of swarmalators inside the vision sphere of the i th swarmalator excluding it [refer to Sec. S1 of the Supplemental Material [45] and Fig. 1 of the manuscript for a derivation of Eq. (1b)]. $\xi_i^x(t)$ and $\xi_i^\sigma(t)$ are the Gaussian white noise with zero mean and strengths d_{x_k} and d_{σ_k} characterized by $\langle \xi_i^{x_k}(t) | \xi_i^{x_k}(t') \rangle = 2d_{x_k} \delta(t - t')$ and $\langle \xi_i^{\sigma_k}(t) | \xi_i^{\sigma_k}(t') \rangle = 2d_{\sigma_k} \delta(t - t')$, respectively, where $k = 1, 2, 3, \dots, D$. Note that σ_i has to be normalized at each time step to ensure it is a unit vector because of $\xi_i^{\sigma_k}(t)$.

Swarmalators in most real-world swarms only exchange interactions with their N_i -nearest neighbors that are within their sphere of influence, resulting in the notion of vision radius. Swarmalators within the vision sphere tend to align their internal state, whereas the others $N_r = N - N_i - 1$ have the natural tendency to repel each other. In the following, we will provide details on the methods involved in the simulation, data visualization, and employed order parameters to characterize various collective dynamical states.

III. METHODS

A. Numerical simulations and visualization

We have numerically solved Eq. (1) using the Runge Kutta fourth-order integration scheme with a step size of 0.1. Initial conditions for the position vectors are randomly drawn from a 3D box of length 2 with each side being uniformly distributed between $[-1, 1]$, and for the orientation vectors they are randomly drawn from the uniform distributions $\theta \in [0, \pi]$ and $\phi \in [0, 2\pi)$. We have fixed $\mathbf{v}_i = \omega_i = 0 \forall i$, $d_{x_k} = d_{\sigma_k} = 0$, $\alpha = 1$, $\beta = 3$, $\gamma = 1$, $N = 100$, and distinct self-organizing behaviors are classified in the (J, R) parameter space in the range of $J \in [-1, 1]$ and $R \in [0, 2]$ throughout the manuscript unless otherwise specified. Note that the parameters α , β , and γ will only affect the equilibrium distance between the swarmalators. Therefore, the states observed in our study can still be observed across different sets of α , β , and γ values, which may slightly shift their spread in the two-parameter phase diagrams.

Each swarmalator is represented by a cone with its apex pointing along the orientation vector. The degree of the

orientation of the i th swarmalator is encoded in σ_i , which is represented using the color code in the heat map in Fig. 1(d). We have used the Mayavi Python package for the 3D visualization of swarmalators. To test the robustness of the collective states observed in our high-dimensional swarmalator model, we have used zero mean white noise with varying noise strengths (d_{x_k}, d_{σ_k}). We have observed that the self-organized states are resilient despite the presence of noise.

B. Order parameters

We have used distinct order parameters to characterize and classify distinct self-organizing collective behaviors (see Table S1). The synchronization order parameter quantifies the degree of coherence among the orientation vectors of the swarmalators, which can be defined as the norm of the average orientation of all the swarmalators, represented as

$$S = \frac{1}{N} \left| \sum_{j=1}^N \sigma_j \right|, \quad (3)$$

where σ_j is the orientation vector of the j th swarmalator. The synchronization order parameter S varies in the range $[0, 1]$. The asynchronized state will have $S = 0$, whereas the synchronized state is characterized by $S = 1$. Intermediate values of S between 0 and 1 quantify the degree of coherence among the orientation vectors.

The orientation parameter quantifies the degree of alignment of the orientation vector of the i th swarmalator with respect to its position vector (see Fig. S1). The orientation parameter used to distinguish distinct spiky states such as a flower state, a twisted state, and a star state can be defined as

$$\Lambda = \frac{1}{N} \sum_{i=1}^N \frac{\mathbf{x}_i \cdot \sigma_i}{|\mathbf{x}_i| |\sigma_i|}, \quad (4)$$

where \mathbf{x}_i is the position vector of the i th swarmalator. The orientation parameter Λ can vary in the range $[-1, 1]$. The star state (see Table S1), in which all swarmalators have orientations pointing radially outwards from the sphere, is characterized by $\Lambda = 1$. An inverted star state (in which all swarmalators would point radially inwards) is characterized by $\Lambda = -1$. Intermediate values of Λ characterize the degree of orientation of the swarmalators in spiky states such as a flower state and a twisted state.

The collective states with a spherical cavity (see Fig. S1) as their core, such as in spiky states and active phase waves, are characterized using the hollowness parameter defined as

$$H = \frac{\min \{|\mathbf{x}_i|\}}{\max \{|\mathbf{x}_i|\}}, \quad i = 1, 2, \dots, N. \quad (5)$$

The hollowness parameter H can vary between 0 and 1. Solid spherical states, such as a static phase wave, and synchronized states are characterized by $H = 0$. Intermediate values of H between 0 and 1 quantify the degree of spherical cavity forming the core of the collective states.

Asymptotically active states are characterized using the kinetic energy parameter defined as

$$E = \frac{1}{N} \sum_{i=1}^N \dot{\mathbf{x}}_i^2. \quad (6)$$

The nonzero values of E indicate that the collective state is dynamic, whereas near-zero values indicate that the collective state is static. The kinetic energy parameter is depicted as a function of time for the spinning cluster, active phase wave, and static synchronized state in Fig. S2.

C. K -means clustering approach

Clustering is one of the interesting intrinsic features of our model. The swarmalators self-organize to form synchronized clusters for suitable parameters. We have used the heuristic elbow curve method [46] in K -means clustering to quantify the number of clusters using the spatial and orientation data.

K -means clustering is an unsupervised machine-learning algorithm that segregates data into K clusters [47,48]. For implementation of this algorithm, the “kmeans” function from the scikit-learn python library is used. The algorithm works by randomly choosing K points called centroids and iteratively reassigning each data point to the cluster whose centroid is closer to it in terms of Euclidean distance. For further iterations, the clusters mean is taken as their new centroid. The process is repeated until the Frobenius norm of the difference in the cluster centers of two consecutive iterations is less than a threshold value.

In particular, the swarmalators are classified based on their locations and phases $X = (x_1, x_2, x_3, \sigma_1, \sigma_2, \sigma_3)$ into clusters $C = \{C_1, C_2, \dots, C_K\}$,

$$\psi = \sum_{K'=1}^K \sum_{i=1}^{N_{K'}} |\mathbf{X}_i^{K'} - \boldsymbol{\mu}^{K'}|^2, \quad (7)$$

where $\boldsymbol{\mu}^{K'}$ is the center of K' cluster, and ψ is the clustering error. We run the K -means clustering algorithm for our data with different values of K ranging from 1 to 20, and we evaluate the clustering error or variance. The intuition is that every increment in the value of K will surely result in a decrease in variance ψ but would have diminishing returns. At some point, when the value of K crosses the true number of clusters, the diminishing returns will be significant enough that it can be seen as an “elbow” in the (K, ψ) plot (see Fig. S3). The elbow point, K_{best} , can be numerically calculated by finding the maximum change of slope $\eta(K)$ in the (K, ψ) plot, where

$$\eta(K) = \left[\frac{\psi(K_{i-1}) - \psi(K_i)}{\psi(K_i) - \psi(K_{i+1})} \right], \text{ and}$$

$$K_{\text{best}} = \text{argmax}_K [\eta(K)].$$

The estimation of the number of clusters from the change of slope of the (K, ψ) plot is depicted in Fig. S3 for two, three, and five clusters. The distinct clusters of the orientation vectors maximize their separation due to the strong repulsive interaction among the clusters constituted by the dissimilarly orientated vectors as shown in their time traces in Fig. S4.

In the following, we will discuss more important types of interactions among the orientation vectors of the swarmalators, while others are presented in the Supplemental Material [45].

IV. RESULTS

A. Competitive interaction

In this section, we will unravel the collective dynamical states that emerge due to the competitive interaction between the attractive and repulsive couplings characterized by $\varepsilon_a = \varepsilon_r$.

1. Characterization of dynamical states

Distinct self-organizing collective behaviors and their dynamical transitions are depicted in Figs. 2(a)–2(c) as a function of the vision radius R for three different values of $J = -0.9, 0.1, \text{ and } 0.9$, respectively, and for $\varepsilon_a = \varepsilon_r = 0.5$. The synchronization order parameter S , hollowness H , kinetic energy E , number of clusters N_c , and orientation parameter Λ including the K -means clustering are used to characterize and classify the distinct collective dynamical states. Note that $N_c \in (1, 5)$ is normalized to $N_c \in (0, 1)$, so that $N_c = 0$ corresponds to a single cluster, $N_c = 0.2$ corresponds to a two-cluster, and so on. In Fig. 2(a), the static asynchronous region in the range of $R \in (0, 0.375]$ for $J = -0.9$ is characterized by the null value of S, E, N_c , and a very small value of $H \approx 0.1$. Since the swarmalators are randomly oriented in the static async (SA) state, the orientation parameter also acquires $\Lambda = 0$. A sudden spike in the value of the kinetic energy parameter at $R = 0.375$ elucidates the active nature of the collective state “active core static spiky state” (ACSPW) in the range of $R \approx (0.375, 1.8]$. In this range of R , the values of the order parameters S, N_c , and H remain very low. The orientation parameter fluctuates about $\Lambda = 0$ from positive to negative values due to the active nature of the core (see the next section for an explanation of the active nature of the core). A turning tube (TT) is observed for $R > 1.8$, which is characterized by a large value of S and H , whereas the parameters Λ, H , and N_c acquire very low values. The snapshots of all these states are depicted in Fig. 3, while all the observed dynamical states in this manuscript are tabulated in Table S1 along with their acronyms.

In Fig. 2(b), there is a transition from SA to static sync (SS) via a spiky state (SP) and a chimera (CH) as a function of R for $J = 0.1$. SA in the range of $R \in (0, 0.375]$ is characterized by near null values of all five parameters, which manifests as SP states as R is increased further. The spiky states consist of flower and twisted states, which are hollow in nature. For instance, see Fig. S5D for the hollow nature of the flower state. The hollowness parameter acquires $H \approx 1$ in the range of $R \in (0.375, 1.4]$, while the orientation parameter takes some finite value. The other parameters in this range of vision radius take very low values near zero. The SP state manifests as a chimera state for $R \in (1.4, 1.8]$. As the latter state is characterized by coexisting coherent and incoherence domains (see Figs. S5E and S6), the synchronization order parameter acquires $S \in (0.2, 0.98)$ in accordance with the degree of the synchronized domain. The hollowness parameter for a CH state acquires

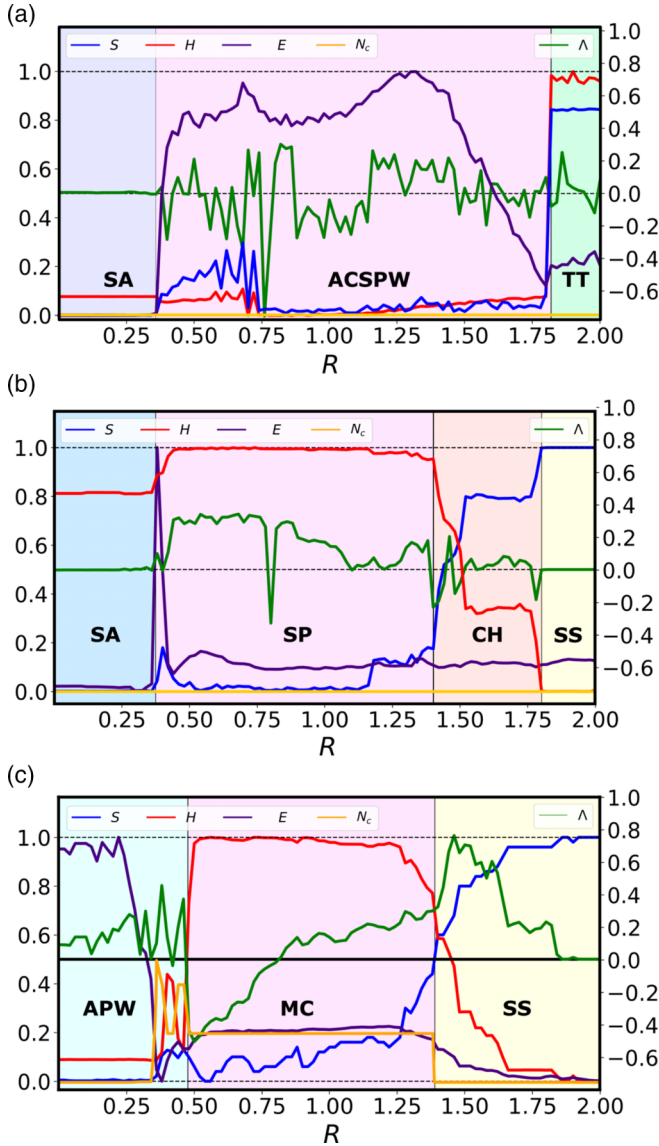


FIG. 2. Dynamical transition using order parameters. The dynamical transitions leading to distinct self-organizing collective behaviors as a function of the vision radius R for (a) $J = -0.9$, (b) $J = 0.1$, and (c) $J = 0.9$. The synchronization order parameter S , hollowness H , kinetic energy E , number of clusters N_c , and orientation parameter Λ are used to characterize and distinguish distinct dynamical states. The parameters are fixed as $\varepsilon_a = \varepsilon_r = 0.5$ and $N = 100$. See the main text for a more detailed explanation.

some finite but rather low value. As R is increased further beyond $R = 1.8$, CH manifests as an SS state characterized by $S = 1$. The other parameters are negligibly small in this range of R . See Fig. S6B for the change in the synchronization order parameter S and the orientation parameter Λ as a function of R corroborating the CH and its transition to an SS state.

In Fig. 2(c), there is a transition from an active phase wave (APW) to SS via the multicluster (MC) state as a function of R for $J = 0.9$. E is rather high characterizing the APW. $N_c = 0.2$ elucidates that the MC is a two-cluster state, while the finite values of the other order parameters in the MC region

characterize the nature of the cluster. For a sufficiently large R , MC manifests as SS as corroborated by a large value of the synchronization order parameter S .

2. Phase diagram

Now, for a global perspective, we unfold the influence of the competitive attractive and repulsive interactions among the orientation vectors on the intriguing self-organizing dynamics in the (J, R) parameter space. Some of the fascinating self-organized convergent multistable symphonies by the swarmalator collectives are depicted and demarcated in Fig. 3. The dynamical regions in the phase diagram are characterized by the order parameters as in Fig. 2. Swarmalators with the angle of inclination $\rho_{ij} \in (\pi/2, \pi)$ (refer to Fig. 1) are strongly attracted for $J < 0$ and hence the collectives display a static async (SA) for small R , as the majority of the swarmalators lie outside R with the tendency to repel each other. Swarmalators with $\rho_{ij} \in (0, \pi/2]$ are attracted strongly for $J > 0$ and exhibit SA for small R and J (see Fig. S7 and refer to the text S2 for its explanation on spatial interaction between two swarmalators). Nevertheless, swarmalators with nearby σ are strongly attracted above appreciable J , even for small R , to self-organize to display a phase wave, which is active (APW) (see Fig. 3) due to the competitive repulsion among the orientation vectors and weak spatial attraction as the majority of them lie outside R .

N_i increases progressively proportional to R resulting in the manifestation of multiclusters (MC) from APW as R is increased, which eventually merges together to manifest as a single static synchronized cluster above a large R as shown in Fig. 3. The sufficient condition for synchronization can be obtained as $R > 1/\sqrt{1-J}$ (see Sec. V for a detailed derivation). Refer to Table S1 for a description of the acronyms for observed states.

Now, each cluster in MC becomes sparse as J is decreased in the intermediate range of R , due to a low degree of spatial attraction, and eventually the MC gather together with their preferred orientation to showcase spiky states. Two such spiky states, namely twisted and flower states, are depicted in Fig. 3, where the orientation vectors are radially pointed outwards from the axis of symmetry in the flower state and vice versa in the twisted state. See Figs. S5F and S8B for a more detailed view of a flower state and a twisted state, respectively. Note that the emergence of SP states is extended even for $J < 0$, although it is sparser than those for $J > 0$, as there lies a net positive spatial attraction for small $|J|$ and hence there is a meager local synchronization for the SP state to persist. Further decrease in J , in the same range of R , facilitates an active core static phase wave with a turbulent core and the outer shell as the SPW.

A strong attraction among the N_r swarmalators for $J < 0$ manifests the asynchronous core, while the synchronized swarmalators within R are weakly attracted, leading to the SPW. Now, the swarmalators in the core that fall within R tend to synchronize and eventually repel outside of R to get asynchronized, which are again attracted, both due to $J < 0$, reinforcing the effect resulting in the active core.

An increase in R from SP for $J > 0$ increases N_i resulting in the synchronized core, and the remaining N_r swarmalators

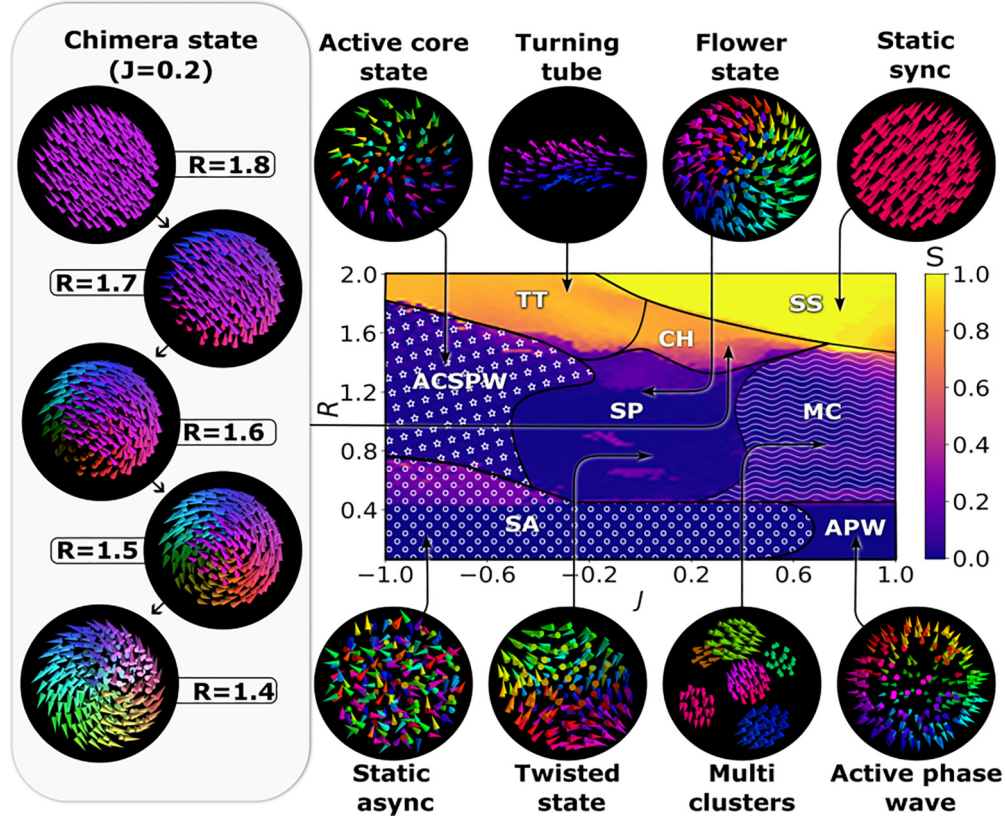


FIG. 3. The synchronization order parameter S is depicted in the two-parameter (J, R) phase diagram for competitive attractive and repulsive interactions for $\varepsilon_a = \varepsilon_r = 0.5$. The left panel depicts the evolution of a chimera state as the vision radius R increases from $R = 1.4$ to 1.8. The snapshots of the swarmalators depicting distinct collective dynamical states are shown in the top and bottom panels. These states are characterized using order parameters (S, Λ, N_c, E, H) .

form a SPW shielding the core. Such a coexistence of coherent and incoherent domains is known as a chimera. The coherent core increases with R and eventually CH manifests as SS for a large R (see Fig. 3). CH and SS transform to a turning tube for $J < 0$, as the spatial attraction among the incoherent domain is stronger, which remains rolling with N_i like the active core in ACSPW.

It is important to emphasize that the observed self-organizing behaviors are robust against Gaussian noise (Fig. S8). Note that the observed collective states displayed by the swarmalators are in the absence of angular velocity $\omega_i = 0$. Nevertheless, we have also unraveled the dynamical states of chiral swarmalators [12] by including angular frequencies. Phase diagrams for two orthogonal angular frequencies ($\omega_1 = [1, 0, 0]$ and $\omega_2 = [0, 1, 0]$ distributed equally among all N swarmalators) and distributed orthogonal angular frequencies are depicted in Figs. S9B and S9C, respectively, for the competitive interaction. Refer to Sec. S4 of the Supplemental Material [45] for the explanation of the latter figures. Emerging dynamical behaviors for the attraction-dominated ($\varepsilon_a > \varepsilon_r$) competitive interaction are depicted in Fig. S10, those for repulsion-dominated ($\varepsilon_r > \varepsilon_a$) competitive interaction are depicted in Fig. S11 for $\omega_i = 0 \forall i$, two orthogonal angular frequencies ($\omega_1 = [1, 0, 0]$ and $\omega_2 = [0, 1, 0]$), and distributed orthogonal angular frequencies. Refer to Secs. S4–S5 of the Supplemental Material [45] for their corresponding

discussions. The heat maps of the employed order parameters corresponding to Figs. S10A–S11A are shown in Fig. S12.

B. Extreme R and local attractive coupling

Swarmalator collectives exclusively display SS (SA) for $N_i = N - 1$ ($N_r = N - 1$) as all of them experience only local attractive (global repulsive) phase coupling [see Fig. 4(a)]. Nevertheless, the collectives exhibit alluring patterns for exclusive local attractive coupling among the orientation vectors as a function of R especially for $J < 0$ [see Fig. 4(a)]. Here, we uncover a transition from SA to SPW in contrast to the transition from SA to APW in the competitive interaction as a function of J in the low range of R as the influence of spatial proximity is absent on the swarmalators that lie outside R . SPW manifests as SS via MC as R is increased for $J > 0$. There is a transition from SA to SS via a mixed synchronized state (MSS) as R is increased for $J < 0$. SS becomes more and more dense (sparse) for $J > 0$ ($J < 0$) [Figs. 4(a), A–D] as the spatial attractive coupling strength increasingly becomes stronger (weaker) as J is increased (decreased). MC of similar sizes are formed for $R = 0.5$ with a weak spatial attraction within the clusters and a strong spatial attraction among the clusters, resulting in the MSS. The size of some of the synchronized clusters increases with R that are spatially

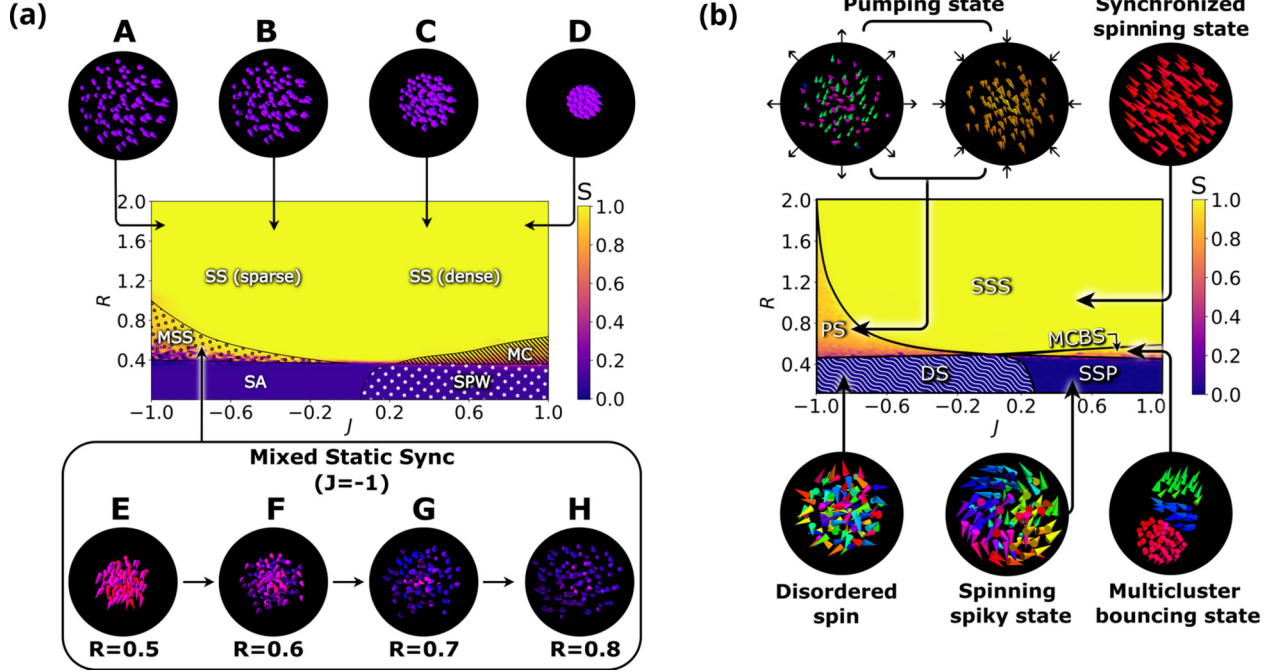


FIG. 4. (a) Synchronization order parameter S is depicted as the heat map for $\varepsilon_a = 0.5$ and $\varepsilon_r = 0$ in the (J, R) space. Refer to the text for details. (b) Swarmalators with orthogonal angular frequencies. Simulations are performed for $N = 100$, $\varepsilon_a = 0.9$, $\varepsilon_r = 0.1$. The pumping state is a dynamic state in which swarmalators compress and expand in a rhythmic pattern.

sparse [see Fig. 4(a), F and G]. See Fig. S13 (S14) and text S6 (S7) for a comparison with two orthogonal angular frequencies, and distributed orthogonal angular frequencies for local attractive coupling (global repulsive coupling).

C. Competitive interaction with quenched disorder

Next, we explore the effect of quenched disorder, $\mathbf{W}_i \sigma_i$, on the swarming dynamics due to the competitive interactions among the orientation vectors. We consider equally distributed orthogonal angular frequencies $\omega_1 = [1, 0, 0]$ and $\omega_2 = [0, 1, 0]$ for sustained precession of the orientation vectors. The swarmalators quench their precession (movie S8) leading to nonchiral collective states as in Figs. 3 and 4(a) for other choices of ω_i . Effectively, $\mathbf{W}_i \sigma_i$ in Eq. (1b) induces a dispersion among the orientation vectors that leads to distinct chiral states with precessing swarmalators [see Fig. 4(b)]. The influence of R and J is similar to that discussed in Fig. 4(a). For low values of R , disordered spin (DS) manifests as spinning spiky (SSP) states above a critical value of $J > 0$. From SSP, a synchronized spinning state (SSS) is formed via a multicluster bouncing spin (MCBS) state as R is increased. A pumping state (PS) mediates the transition from DS to SSS. The density of SSS decreases as $J \rightarrow -1$ as in Fig. 4(a). Precessing orientation vectors recursively result in their coherence and decoherence, which dynamically establishes dense and sparse synchronized clusters, respectively. The dense clusters repel each other, whereas the swarmalators in the sparse clusters that fall within their R are synchronized, resulting in the reinforcement of MCBS for $J > 0$. A similar mechanism underlies the onset of PS for $J < 0$, where recursive coherence and decoherence result in sparse synchronous

and dense asynchronous collectives dynamically resulting in the PS.

V. THEORETICAL ANALYSIS

A. Maximal separation between two clusters

The maximal distance between the two-cluster state can be deduced in the limit of large J as follows. Let ζ_A, ζ_B be the two populations of the swarmalator collectives that form two clusters A and B , respectively, and let N_A, N_B be their respective cardinal numbers. In steady state, the mean velocity of each cluster is zero, and consequently the sum of the velocities of all the swarmalators constituting the cluster A can be expressed as

$$\sum_{i \in \zeta_A} \dot{\mathbf{x}}_i = \frac{1}{N-1} \sum_{i \in \zeta_A} \sum_{j=1}^N \left[\frac{1 + J(\sigma_i \cdot \sigma_j)}{|\mathbf{x}_{ij}|^\alpha} - \frac{1}{|\mathbf{x}_{ij}|^\beta} \right] \mathbf{x}_{ij}.$$

The second summation can be explicitly expanded as intracuster and intercluster interactions as

$$\sum_{i \in \zeta_A} \sum_{j \in \zeta_A} \left[\frac{1 + J(\sigma_i \cdot \sigma_j)}{|\mathbf{x}_{ij}|^\alpha} - \frac{1}{|\mathbf{x}_{ij}|^\beta} \right] \mathbf{x}_{ij} + \sum_{i \in \zeta_A} \sum_{j \in \zeta_B} \left[\frac{1 + J(\sigma_i \cdot \sigma_j)}{|\mathbf{x}_{ij}|^\alpha} - \frac{1}{|\mathbf{x}_{ij}|^\beta} \right] \mathbf{x}_{ij} = 0. \quad (8)$$

The first term in the above summation corresponds to the interaction within the cluster A , whereas the second term in the summation corresponds to the interaction between the clusters A and B . Representing the first and second summations as A_1

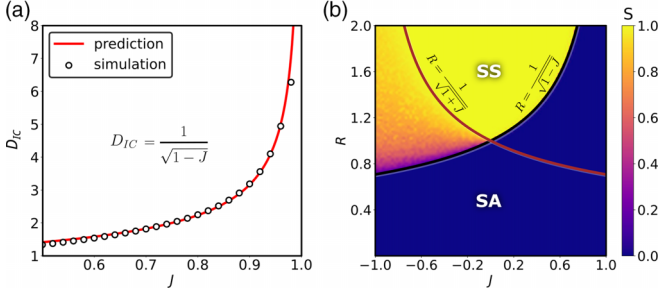


FIG. 5. Dynamics of two swarmalators. (a) Cluster separation of a two-cluster state with varying J . The solid red line is the analytical prediction, and the open circles are the simulation result. (b) Dynamics of the swarmalator model for $N = 2$ for competitive interaction among the orientation vectors. The heat map illustrates the synchronization order parameter estimated from the evolution of the orientation vectors. The sufficient condition for synchronization was shown to be $R > |\mathbf{x}_{12}| = 1/\sqrt{1+J(\boldsymbol{\sigma}_1 \cdot \boldsymbol{\sigma}_2)}$. The analytical critical curve $R = 1/\sqrt{1 \pm J}$, depicted in the figure, agrees well with the simulation results.

and A_2 , respectively,

$$A_1 = \sum_{i \in \zeta_A} \sum_{j \in \zeta_A, j \neq i} \frac{\mathbf{x}_{ij} + \mathbf{x}_{ji}}{2} \left[\frac{1 + J(\boldsymbol{\sigma}_i \cdot \boldsymbol{\sigma}_j)}{|\mathbf{x}_{ij}|^\alpha} - \frac{1}{|\mathbf{x}_{ij}|^\beta} \right]. \quad (9)$$

Since $A_1 = 0$, following (8) and (9), $A_2 = 0$. Let D_{IC} be the intercluster distance, such that $|\mathbf{x}_{AB}| \approx D_{IC}$,

$$\Rightarrow A_2 = \sum_{i \in \zeta_A} \sum_{j \in \zeta_B} \left[\frac{1 + J(\boldsymbol{\sigma}_i \cdot \boldsymbol{\sigma}_j)}{D^\alpha} - \frac{1}{D^\beta} \right] \mathbf{x}_{ij}.$$

Since swarmalators within both clusters A and B are synchronized, $\boldsymbol{\sigma}_i = \boldsymbol{\sigma}_A$ and $\boldsymbol{\sigma}_j = \boldsymbol{\sigma}_B \forall i \in \zeta_A$ and $j \in \zeta_B$,

$$\Rightarrow A_2 = \left[\frac{1 + J(\boldsymbol{\sigma}_A \cdot \boldsymbol{\sigma}_B)}{D_{IC}^\alpha} - \frac{1}{D_{IC}^\beta} \right] \sum_{i \in \zeta_A} \sum_{j \in \zeta_B} \mathbf{x}_{ij}.$$

Since $A_2 = 0$ and $\sum_{i \in \zeta_A} \sum_{j \in \zeta_B} \mathbf{x}_{ij} \neq 0$, one can obtain the intercluster distance as

$$D_{IC}^{\beta-\alpha} = \frac{1}{1 + J(\boldsymbol{\sigma}_A \cdot \boldsymbol{\sigma}_B)}.$$

For the chosen values of the parameters $\alpha = 1$ and $\beta = 3$, the intercluster distance turns out to be

$$D_{IC} = \frac{1}{\sqrt{1 + J(\boldsymbol{\sigma}_A \cdot \boldsymbol{\sigma}_B)}}.$$

Maximal cluster separation is obtained when $\boldsymbol{\sigma}_A \cdot \boldsymbol{\sigma}_B = -1$. Analogously, minimal cluster separation can be obtained when $\boldsymbol{\sigma}_A \cdot \boldsymbol{\sigma}_B = 1$. Accordingly, the maximal and minimal separation between the two clusters are $D_{\max} = 1/\sqrt{1-J}$ and $D_{\min} = 1/\sqrt{1+J}$, respectively. Since clusters would surely merge and synchronize once $R > D_{\max}$, the sufficient condition for the emergence of static sync turns out to be $R > 1/\sqrt{1-J}$, which is numerically verified in Fig. 5(a), and the analytical estimate matches well with the simulation results.

B. Dynamics of two swarmalators

The equation of motion for the spatial dynamics in the case of two swarmalators is represented as

$$\begin{aligned} \dot{\mathbf{x}}_1 &= \{1 + J(\boldsymbol{\sigma}_1 \cdot \boldsymbol{\sigma}_2)\} \frac{\mathbf{x}_2 - \mathbf{x}_1}{|\mathbf{x}_2 - \mathbf{x}_1|^\alpha} - \frac{\mathbf{x}_2 - \mathbf{x}_1}{|\mathbf{x}_2 - \mathbf{x}_1|^\beta}, \\ \dot{\mathbf{x}}_2 &= \{1 + J(\boldsymbol{\sigma}_2 \cdot \boldsymbol{\sigma}_1)\} \frac{\mathbf{x}_1 - \mathbf{x}_2}{|\mathbf{x}_1 - \mathbf{x}_2|^\alpha} - \frac{\mathbf{x}_1 - \mathbf{x}_2}{|\mathbf{x}_1 - \mathbf{x}_2|^\beta}. \end{aligned}$$

The evolution equations governing the dynamics of orientation vector (internal states) are given as

$$\begin{aligned} \dot{\boldsymbol{\sigma}}_1 &= k_{12} \left[\frac{\boldsymbol{\sigma}_2 - (\boldsymbol{\sigma}_2 \cdot \boldsymbol{\sigma}_1) \boldsymbol{\sigma}_1}{|\mathbf{x}_2 - \mathbf{x}_1|^\gamma} \right], \\ \dot{\boldsymbol{\sigma}}_2 &= k_{21} \left[\frac{\boldsymbol{\sigma}_1 - (\boldsymbol{\sigma}_1 \cdot \boldsymbol{\sigma}_2) \boldsymbol{\sigma}_2}{|\mathbf{x}_1 - \mathbf{x}_2|^\gamma} \right]. \end{aligned}$$

For spatially static steady states, $\dot{\mathbf{x}}_1 = 0$ and $\dot{\mathbf{x}}_2 = 0$, and therefore the equation of motion corresponding to the spatial dynamics can be expressed as

$$\frac{\mathbf{x}_2 - \mathbf{x}_1}{|\mathbf{x}_2 - \mathbf{x}_1|^\alpha} \left[\{1 + J(\boldsymbol{\sigma}_1 \cdot \boldsymbol{\sigma}_2)\} - \frac{1}{|\mathbf{x}_2 - \mathbf{x}_1|^{\beta-\alpha}} \right] = 0.$$

Since $(\mathbf{x}_1 - \mathbf{x}_2) \neq 0$, we get

$$|\mathbf{x}_2 - \mathbf{x}_1|^{\beta-\alpha} = \frac{1}{1 + J(\boldsymbol{\sigma}_1 \cdot \boldsymbol{\sigma}_2)}. \quad (10)$$

Substituting the above for the spatial separation between the two swarmalators in the evolution equation for the orientation vectors, the latter can be expressed only in terms of the orientation vectors as

$$\begin{aligned} \dot{\boldsymbol{\sigma}}_1 &= k[1 + J(\boldsymbol{\sigma}_1 \cdot \boldsymbol{\sigma}_2)]^{\frac{\gamma}{\beta-\alpha}} [\boldsymbol{\sigma}_2 - (\boldsymbol{\sigma}_1 \cdot \boldsymbol{\sigma}_2) \boldsymbol{\sigma}_1], \\ \dot{\boldsymbol{\sigma}}_2 &= k[1 + J(\boldsymbol{\sigma}_1 \cdot \boldsymbol{\sigma}_2)]^{\frac{\gamma}{\beta-\alpha}} [\boldsymbol{\sigma}_1 - (\boldsymbol{\sigma}_1 \cdot \boldsymbol{\sigma}_2) \boldsymbol{\sigma}_2]. \end{aligned}$$

The above equations completely describe the static states. Note that Eq. (10) turns out to be the exact separation between the two clusters, $D_{IC} = 1/\sqrt{1-J}$. Here, in the case of two swarmalators, the sufficient condition for synchronization is exactly the same as that deduced from the two-cluster state. Two swarmalators can display a static sync (SS), static asyc (SA), and static phase wave, which cannot be distinguished from SA. In the region described by the condition $1/\sqrt{1-J} < R < 1/\sqrt{1+J}$ [see Fig. 5(b)], the swarmalators will have intermediate synchronization in the negative J region due to oscillations arising from the alternative synchronization and desynchronization when they enter and leave the vision radius.

VI. SELF-PROPELLED SWARMALATORS

In this section, we describe the collective dynamics of self-propelled swarmalators ($v_i \neq 0$). Vicsek's model has been widely used to describe phase transitions in the system of self-propelled particles, although the model is based on simple interaction rules and nicely captures the flocking behavior of birds, fish, and bacterial swarming. The coherent state arises in the case of high density, and the direction of motion is inherently the direction of orientation. In contrast,

the Kuramoto model based orientation (phase) dynamics is advantageous in that it can control the synchronization by varying the coupling strength between agents. Additionally, the swarmalator model can treat the orientation and the direction of movement independently, which can play a crucial role in more advanced systems such as a swarm of drones [49] and microrobot collectives [38]. The orientation vector can be any system variable that needs to be synchronized to facilitate cooperation (e.g., swarm-based sensing and tracking [50]) among agents. In the context of drones, σ_i can be orientation sensors, a camera, actuators, or it can be the physical orientation of the drone itself, while in magnetic microrobots the orientation may represent the direction of polarity. The self-organizing behavior of swarmalators can be utilized in performing specific coordinated operations by tuning suitable parameters.

Schooling of fish

To elucidate that the swarmalators can capture flocking behavior, we display the defensive maneuver of a real school of fish by including self-propelling velocity and modifying the repulsive interaction among the orientation vectors to include the centripetal inclination of the fish towards their center of mass to evade predation. These collective behaviors offer several advantages, such as enhanced predator defense and increased foraging efficiency [51]. The orientation vector describing the internal state of a swarmalator can be interpreted as the heading direction of the swarmalator (fish). We choose the self-propulsion velocity along the orientation of the agent as

$$\mathbf{v}_i = c_i \sigma_i,$$

where c_i is the mapping coefficient for self-propulsion velocity. Hence the spatial dynamics in Eq. (1) can be modified as

$$\begin{aligned} \dot{\mathbf{x}}_i = & c_i \sigma_i + \frac{1}{N-1} \sum_{j=1}^N \{1 + J(\sigma_i \cdot \sigma_j)\} \frac{\mathbf{x}_j - \mathbf{x}_i}{|\mathbf{x}_j - \mathbf{x}_i|^\alpha} \\ & - \frac{\mathbf{x}_j - \mathbf{x}_i}{|\mathbf{x}_j - \mathbf{x}_i|^\beta} + \xi_i^x(t). \end{aligned} \quad (11)$$

Bait-ball or milling of a school of fish maintains their social boundary with some radius L with respect to their center of mass.

During schooling, fish maneuver their orientation such that they stay inside this social structure (L) to increase their chance of survival [52]. The evolution equation corresponding to the orientation vector can be represented as

$$\dot{\sigma}_i = \mathbf{W}_i \sigma_i + \sum_{j=1}^N \frac{\varepsilon_a}{N_i} \left[\frac{\sigma_j - (\sigma_j \cdot \sigma_i) \sigma_i}{|\mathbf{x}_j - \mathbf{x}_i|^\gamma} \right] - \mathbf{F}_i. \quad (12)$$

Note that $\mathbf{W}_i = \mathbf{0}$, and the repulsive coupling among the orientation vectors in Eq. (1) is replaced by the term \mathbf{F}_i , which is expressed as

$$\mathbf{F}_i = \frac{\mathbf{x}_i^c - (\mathbf{x}_i^c \cdot \sigma_i) \sigma_i}{|L \hat{\mathbf{x}}_i^c - \mathbf{x}_i^c|}, \quad (13)$$

where $\mathbf{x}_i^c = \mathbf{x}_i - \mathbf{x}_c$ represents the position of the i th swarmalator with respect to their center of mass, $\mathbf{x}_c = \sum_{i=1}^N \mathbf{x}_i / N$. The term \mathbf{F}_i can be considered as the force that enforces the centripetal inclination of the school of fish, which makes it possible for them to maintain the dense bait-ball formation to evade their predators [53]. Typical configurations observed during the schooling of fish are the swarm state, the polarized state, and the milling state. In the case of milling, swarmalators (here fish) show coordinated rotational motion, and in a polarized (crystal) state the fish are aligned.

We have used the experimental data [54] to depict the snapshots of crystal and milling behavior [55,56] of a school of fish in Figs. 6(a) and 6(c). The self-organizing dynamics of our model mimic very well the observed crystal and milling behaviors as depicted in Figs. 6(b) and 6(d), respectively. To quantitatively describe the observed collective behaviors of a school of fish, we use three order parameters, namely a synchronization parameter (S), spatial vorticity (Γ_x), and phase vorticity (Γ_σ). The synchronization parameter provides the measurement of the alignment of individuals in the group. To measure the rotational motion of the fish, we use vorticity parameters [57]. Spatial vorticity (Γ_x) is calculated using spatial velocity, and it is useful for capturing the vorticity arising due to the lateral motion, while the phase vorticity is calculated using the orientation vectors, and it is useful for measuring the vorticity due to motion along the heading direction. The spatial vorticity is defined as

$$\Gamma_x = \frac{1}{N} \left| \sum_i^N \hat{\mathbf{x}}_i^c \times \hat{\mathbf{v}}_i \right|, \quad (14)$$

where $\hat{\mathbf{x}}_i^c$ is the unit vector corresponding to the position vector of the i th swarmalator with respect to their center of mass \mathbf{x}_c , and $\hat{\mathbf{v}}_i$ is the unit vector of the spatial velocity of the i th swarmalator. Phase vorticity is defined as

$$\Gamma_\sigma = \frac{1}{N} \left| \sum_i^N \hat{\mathbf{x}}_i^c \times \sigma_i \right|. \quad (15)$$

Both vorticity parameters, Γ_x and Γ_σ , can vary in the range 0–1. Quantitatively, the milling state is characterized by high vorticity ($\Gamma_x \approx 1, S \approx 0$), while the polarized state is characterized by the high value of the synchronized parameters ($S \approx 1, \Gamma_x \approx 0$). In the swarm state the fish are not ordered, nor do they form vorticity, and hence this state is characterized by feeble spatial and phase vorticities ($\Gamma_x \approx 0, \Gamma_\sigma \approx 0$) and a negligible value of the synchronization order parameter ($S \approx 0$).

The synchronization S and the spatial vorticity Γ_x order parameters, for both the experimental and the simulation data [see movies S25 (simulation) and S26 (experiment) depicting the evolution of the dynamical states and the order parameters], are shown in Figs. 6(e) and 6(f) (Fig. S15), respectively. Heat maps of the order parameters in (J, R) space are shown in Figs. S16 and S17. The null value of $S(\Gamma_x)$ and the unit value of $\Gamma_x(S)$ corroborate the milling (crystal) behavior for

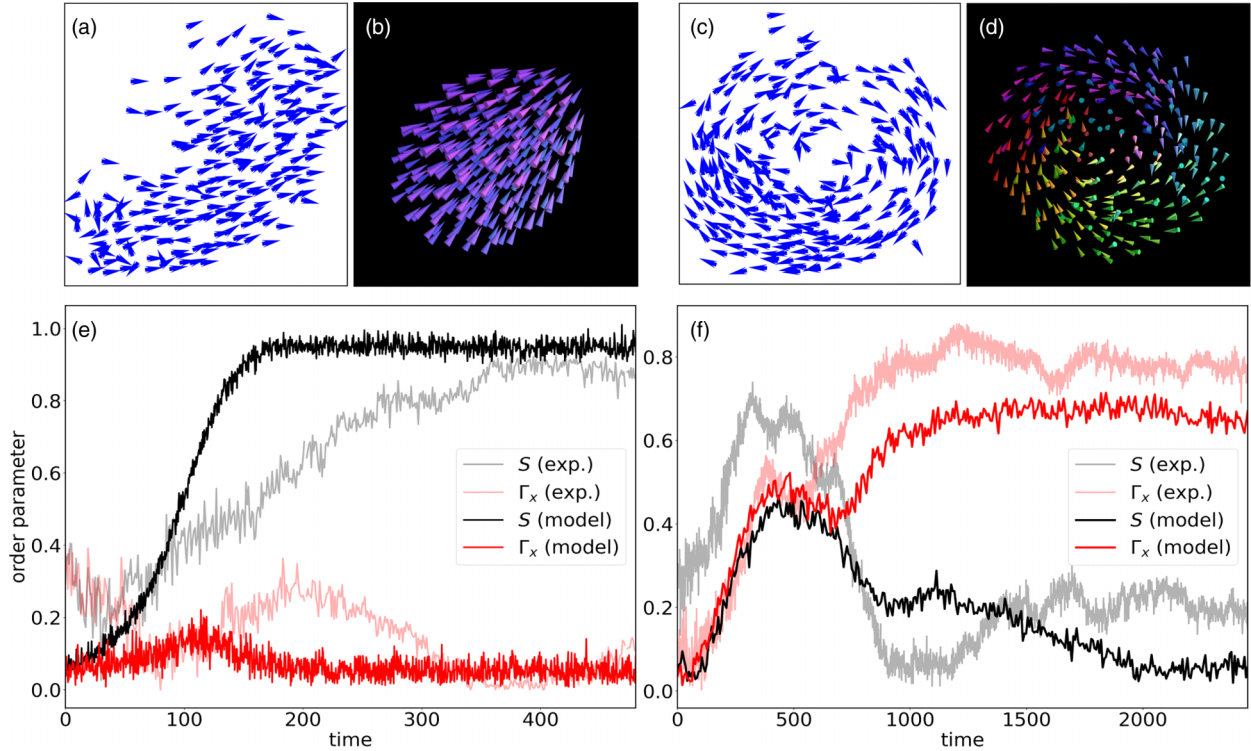


FIG. 6. Real-world parallels. (a) Experimentally observed [54] polarized (crystal) state for 300 golden shiners in shallow water at $t = 330$. (b) Polarized state in our swarmalator model for $N = 300$, $R = 1.0$, $J = 0.7$, $\varepsilon_a = 0.9$, $\varepsilon_r = 0$. (c) Experimentally observed milling state at $t = 1450$. (d) Milling state observed in the proposed swarmalator model for $N = 300$, $R = 0.2$, $J = 0.3$, $\varepsilon_a = 0.7$, $\varepsilon_r = 0$. (e), (f) Time evolution of synchronization (S) and spatial vorticity (Γ_x) order parameters characterizing polarized and milling states, respectively, from both experimental [$S(\text{expt})$ and $\Gamma_x(\text{expt})$] and model [$S(\text{model})$ and $\Gamma_x(\text{model})$] data with noise strength ($d_{x_k} = 0.005$, $d_{\sigma_k} = 0.005$).

$t > 300$ ($t > 700$) in Fig. 6(e) [Fig. 6(f)]. The striking similarities of S and Γ_x for both the experimental and the model data establish the significance of our model in predicting very well the dynamics of a school of fish both qualitatively and quantitatively.

VII. DISCUSSION

We have proposed a D -dimensional swarmalator model and unveiled a rich variety of multistable collective behaviors, tabulated in Table S1 of the Supplemental Material [45], in the phase diagrams. Most of these collective behaviors are manifested only in the proposed generalized model (1), where as only some of them are reported in the literature. We have defined suitable order parameters to characterize and classify the distinct self-organized collective states. As pointed out, the SPW and APW qualitatively resemble the “asters” observed in magnetic colloids and the “vortex arrays” formed by populations of spermatozoa, respectively. Notably, spiky states bear a striking resemblance to the “skyrmions” observed in magnetic materials [58], which are a potential candidate for future data-storage solutions and other spintronics devices. It is likely that other detected behaviors may be identified in several real-world systems. The qualitative resemblance will set the stage for a deeper theoretical investigation of the minimalistic swarmalator model with essential extensions.

We have provided evidence of our model’s strong potential. In particular, we have extended the original model

to successfully capture the schooling behavior of fish. We strongly believe that our model can be used to unfold the underlying mechanism behind self-organizing properties of micro- and nanoswimmers, self-propelling agents, microrobot collectives, etc. In particular, the transportation properties of microrobot collectives can be better controlled using our model for more precise drug delivery and other biomedical applications. Furthermore, strategic formation by drones and precise control of their collective functions using our model can be used for security purposes, rescue operations, explorations, etc. There may be a specific interest in studying reconfigurable microrobots for potential applications, including understanding self-healing structures.

ACKNOWLEDGMENTS

A.Y. acknowledges the financial support from IISER-TVM. The work of V.K.C. is supported by DST-CRG Project under Grant No. CRG/2020/004353, and V.K.C. wishes to thank DST, New Delhi for computational facilities under the DST-FIST programme (SR/FST/PS- 1/2020/135) to the Department of Physics. D.V.S. is supported by the DST-SERB-CRG Project under Grant No. CRG/2021/000816.

A.Y. and K.J. contributed equally to the simulations, analysis, and original draft writing. V.K.C., D.V.S., W.Z., and J.K. contributed to conceptualization, validation, and the review and editing of the work. D.V.S. helped to supervise the project.

- [1] J. Ross and A. P. Arkin, Complex Systems: From chemistry to systems biology, *Proc. Natl. Acad. Sci. USA* **106**, 6433 (2009).
- [2] M. A. Muñoz, *Colloquium: Criticality and dynamical scaling in living systems*, *Rev. Mod. Phys.* **90**, 031001 (2018).
- [3] J. Fan, J. Meng, J. Ludescher, X. Chen, Y. Ashkenazy, J. Kurths, S. Havlin, and H. J. Schellnhuber, Statistical physics approaches to the complex Earth system, *Phys. Rep.* **896**, 1 (2021).
- [4] N. Boers, B. Goswami, A. Rheinwalt, B. Bookhagen, B. Hoskins, and J. Kurths, Complex networks reveal global pattern of extreme-rainfall teleconnections, *Nature (London)* **566**, 373 (2019).
- [5] R. Pastor-Satorras, C. Castellano, P. Van Mieghem, and A. Vespignani, Epidemic processes in complex networks, *Rev. Mod. Phys.* **87**, 925 (2015).
- [6] Y.-Y. Liu, J.-J. Slotine, and A.-L. Barabási, Controllability of complex networks, *Nature (London)* **473**, 167 (2011).
- [7] V. Grimm, E. Revilla, U. Berger, F. Jeltsch, W. M. Mooij, S. F. Railsback, H.-H. Thulke, J. Weiner, T. Wiegand, and D. L. DeAngelis, Pattern-oriented modeling of agent-based complex systems: Lessons from ecology, *Science* **310**, 987 (2005).
- [8] S. A. Levin, H. V. Milner, and C. Perrings, The dynamics of political polarization, *Proc. Natl. Acad. Sci. USA* **118**, e2116950118 (2021).
- [9] V. Sekara, A. Stopczynski, and S. Lehmann, Fundamental structures of dynamic social networks, *Proc. Natl. Acad. Sci. USA* **113**, 9977 (2016).
- [10] K. P. O' Keeffe, H. Hong, and S. H. Strogatz, Oscillators that sync and swarm, *Nat. Commun.* **8**, 1504 (2017).
- [11] G. K. Sar, S. N. Chowdhury, M. Perc, and D. Ghosh, Swarmalators under competitive time-varying phase interactions, *New J. Phys.* **24**, 043004 (2022).
- [12] S. Ceron, K. O' Keeffe, and K. Petersen, Diverse behaviors in non-uniform chiral and non-chiral swarmalators, *Nat. Commun.* **14**, 940 (2023).
- [13] F. Jiménez-Morales, Oscillatory behavior in a system of swarmalators with a short-range repulsive interaction, *Phys. Rev. E* **101**, 062202 (2020).
- [14] P. Japón, F. Jiménez-Morales, and F. Casares, Intercellular communication and the organization of simple multicellular animals, *Cells Develop.* **169**, 203726 (2022).
- [15] N. Blum, A. Li, K. O' Keeffe, and O. Kogan, Swarmalators with delayed interactions, *Phys. Rev. E* **109**, 014205 (2024).
- [16] S. Yoon, K. P. O. Keeffe, J. F. F. Mendes, and A. V. Goltsev, Sync and swarm: Solvable model of nonidentical swarmalators, *Phys. Rev. Lett.* **129**, 208002 (2022).
- [17] G. K. Sar, D. Ghosh, and K. O' Keeffe, Pinning in a system of swarmalators, *Phys. Rev. E* **107**, 024215 (2023).
- [18] O. A. Igoshin, A. Mogilner, R. D. Welch, D. Kaiser, and G. Oster, Pattern formation and traveling waves in myxobacteria: Theory and modeling, *Proc. Natl. Acad. Sci. USA* **98**, 14913 (2001).
- [19] D. Tanaka, General chemotactic model of oscillators, *Phys. Rev. Lett.* **99**, 134103 (2007).
- [20] M. Iwasa, K. Iida, and D. Tanaka, Various collective behavior in swarm oscillator model, *Phys. Lett. A* **376**, 2117 (2012).
- [21] D. Levis and B. Liebchen, Simultaneous phase separation and pattern formation in chiral active mixtures, *Phys. Rev. E* **100**, 012406 (2019).
- [22] D. Levis, I. Pagonabarraga, and B. Liebchen, Activity induced synchronization: Mutual flocking and chiral self-sorting, *Phys. Rev. Res.* **1**, 023026 (2019).
- [23] I. H. Riedel, K. Kruse, and J. Howard, A self-organized vortex array of hydrodynamically entrained sperm cells, *Science* **309**, 300 (2005).
- [24] J.-M. Swiecicki, O. Sliusarenko, and D. B. Weibel, From swimming to swarming: *Escherichia coli* cell motility in two-dimensions, *Integrative Biol.* **5**, 1490 (2013).
- [25] Y. Sumino, K. H. Nagai, Y. Shitaka, D. Tanaka, K. Yoshikawa, H. Chaté, and K. Oiwa, Large-scale vortex lattice emerging from collectively moving microtubules, *Nature (London)* **483**, 448 (2012).
- [26] K. Han, G. Kokot, O. Tovkach, A. Glatz, I. S. Aranson, and A. Snezhko, Emergence of self-organized multivortex states in flocks of active rollers, *Proc. Natl. Acad. Sci. USA* **117**, 9706 (2020).
- [27] J. Yan, S. C. Bae, and S. Granick, Rotating crystals of magnetic Janus colloids, *Soft Matter* **11**, 147 (2015).
- [28] A. Barciś and C. Bettstetter, Sandsbots: Robots that sync and swarm, *IEEE Access* **8**, 218752 (2020).
- [29] M. Z. Miskin, A. J. Cortese, K. Dorsey, E. P. Esposito, M. F. Reynolds, Q. Liu, M. Cao, D. A. Muller, P. L. McEuen, and I. Cohen, Electronically integrated, mass-manufactured, microscopic robots, *Nature (London)* **584**, 557 (2020).
- [30] M. S. Talamali, A. Saha, J. A. R. Marshall, and A. Reina, When less is more: Robot swarms adapt better to changes with constrained communication, *Sci. Robot.* **6**, eabf1416 (2021).
- [31] A. Snezhko and I. S. Aranson, Magnetic manipulation of self-assembled colloidal asters, *Nat. Mater.* **10**, 698 (2011).
- [32] C. Tsiaris and A. Aulehla, Self-organization of embryonic genetic oscillators into spatiotemporal wave patterns, *Cell* **164**, 656 (2016).
- [33] K. Uriu and L. G. Morelli, Determining the impact of cell mixing on signaling during development, *Dev. Growth Differ.* **59**, 351 (2017).
- [34] B. Zhang, A. Sokolov, and A. Snezhko, Reconfigurable emergent patterns in active chiral fluids, *Nat. Commun.* **11**, 4401 (2020).
- [35] L. Song, S. M. Nadkarni, H. U. Bödeker, C. Beta, A. Bae, C. Franck, W.-J. Rappel, W. F. Loomis, and E. Bodenschatz, *Dictyostelium discoideum* chemotaxis: Threshold for directed motion, *Eur. J. Cell Biol.* **85**, 981 (2006).
- [36] L. B. Wong, I. F. Miller, and D. B. Yeates, Nature of the mammalian ciliary metachronal wave, *J. Appl. Physiol.* **75**, 458 (1993).
- [37] J. Elgeti and G. Gompper, Emergence of metachronal waves in cilia arrays, *Proc. Natl. Acad. Sci. USA* **110**, 4470 (2013).
- [38] G. Gardi, S. Ceron, W. Wang, K. Petersen, and M. Sitti, Micro-robot collectives with reconfigurable morphologies, behaviors, and functions, *Nat. Commun.* **13**, 2239 (2022).
- [39] S. Ceron, G. Gardi, K. Petersen, and M. Sitti, Programmable self-organization of heterogeneous microrobot collectives, *Proc. Natl. Acad. Sci. USA* **120**, e2221913120 (2023).
- [40] J. A. Acebrón, L. L. Bonilla, C. J. Pérez Vicente, F. Ritort, and R. Spigler, The Kuramoto model: A simple paradigm for synchronization phenomena, *Rev. Mod. Phys.* **77**, 137 (2005).
- [41] A. Kaiser, A. Snezhko, and I. S. Aranson, Flocking ferromagnetic colloids, *Sci. Adv.* **3**, e1601469 (2017).

- [42] T. Vicsek, A. Czirók, E. Ben-Jacob, I. Cohen, and O. Shochet, Novel type of phase transition in a system of self-driven particles, *Phys. Rev. Lett.* **75**, 1226 (1995).
- [43] S. Chandra, M. Girvan, and E. Ott, Continuous versus discontinuous transitions in the D -dimensional generalized kuramoto model: Odd D is different, *Phys. Rev. X* **9**, 011002 (2019).
- [44] K. Kovalenko, X. Dai, K. Alfaro-Bittner, A. M. Raigorodskii, M. Perc, and S. Boccaletti, Contrarians synchronize beyond the limit of pairwise interactions, *Phys. Rev. Lett.* **127**, 258301 (2021).
- [45] See Supplemental Material at <http://link.aps.org/supplemental/10.1103/PhysRevE.109.044212> for the derivation of the model, a detailed discussion on spatial interaction between two swarms, competitive interaction ($\varepsilon_a = \varepsilon_r$), attraction-dominated competitive interactions ($\varepsilon_a > \varepsilon_r$), repulsion-dominated competitive interaction ($\varepsilon_r > \varepsilon_a$), local attractive coupling, and global repulsive coupling. The Supplemental Material contains Figs. S1–S17 and a description of Movies S1–S26. The gallery of observed self-organizing collective states in the wide range of parameters is shown in Table S1.
- [46] H. Humaira and R. Rasyidah, Determining the appropriate cluster number using Elbow method for K-means algorithm, in *Proceedings of the 2nd Workshop on Multidisciplinary and Applications (WMA) 2018, Padang, Indonesia, Jan 24–25 2018 (EAI) (European Alliance for Innovation, Padang, Indonesia, 2020)*.
- [47] J. A. Hartigan and M. A. Wong, Algorithm AS 136: A K-means clustering algorithm, *J. R. Statist. Soc. Ser. C* **28**, 100 (1979).
- [48] T. Kanungo, D. M. Mount, N. S. Netanyahu, C. D. Piatko, R. Silverman, and A. Y. Wu, An efficient k-means clustering algorithm: analysis and implementation, *IEEE Trans. Pattern Anal. Machine Intell.* **24**, 881 (2002).
- [49] J. Markdahl, D. Proverbio, and J. Goncalves, Robust synchronization of heterogeneous robot swarms on the sphere, in *2020 59th IEEE Conference on Decision and Control (CDC), Jeju, Korea (South) (IEEE, Piscataway, NJ, 2020)*, pp. 5798–5803.
- [50] R. J. Amala Arokia Nathan, I. Kurmi, and O. Bimber, Drone swarm strategy for the detection and tracking of occluded targets in complex environments, *Commun. Eng.* **2**, 55 (2023).
- [51] A. Berdahl, C. J. Torney, C. C. Ioannou, J. J. Faria, and I. D. Couzin, Emergent sensing of complex environments by mobile animal groups, *Science* **339**, 574 (2013).
- [52] C. C. Ioannou, V. Guttal, and I. D. Couzin, Predatory fish select for coordinated collective motion in virtual prey, *Science* **337**, 1212 (2012).
- [53] W. D. Hamilton, Geometry for the selfish herd, *J. Theor. Biol.* **31**, 295 (1971).
- [54] Y. Katz, K. Tunstrøm, C. C. Ioannou, C. Huepe, and I. D. Couzin, *Fish Schooling Data Subset* (Oregon State University, Corvallis, OR, 2021).
- [55] D. Strömbom, M. Siljestam, J. Park, and D. J. Sumpter, The shape and dynamics of local attraction, *Eur. Phys. J. Spec. Top.* **224**, 3311 (2015).
- [56] U. Lopez, J. Gautrais, I. D. Couzin, and G. Theraulaz, From behavioural analyses to models of collective motion in fish schools, *Interface Focus* **2**, 693 (2012).
- [57] K. Tunstrøm, Y. Katz, C. C. Ioannou, C. Huepe, M. J. Lutz, and I. D. Couzin, Collective states, multistability and transitional behavior in schooling fish, *PLoS Comput. Biol.* **9**, e1002915 (2013).
- [58] B. Göbel, I. Mertig, and O. A. Tretiakov, Beyond skyrmions: Review and perspectives of alternative magnetic quasiparticles, *Phys. Rep.* **895**, 1 (2021).